RSC Advances

PAPER

View Article Online
View Journal | View Issue

Cite this: *RSC Adv.*, 2026, **16**, 18624

$CuGaSe_2$ photosensitive devices: a study of reliability and photoresponse with defects

Kavin Malar U, Sneha Aich and Soumyaranjan Routray *

Received 18th January 2026
Accepted 24th March 2026

DOI: 10.1039/d6ra00453a

rsc.li/rsc-advances

$CuGaSe_2$($CGSe_2$) is the material of choice for future generation photosensitive devices such as solar cells due to its high absorption coefficient and band gap. This material was immediately evaluated to determine its suitability as a photovoltaic material. In this article, this material with the simple structure of ZnO/CdS/$CuGaSe_2$ was explored using Silvaco TCAD software. The thickness of all layers was optimized to achieve higher efficiency. The maximum achievable efficiency for the device was recorded to be 30.59%, with a current density (J_{SC}) of 28.03 mA cm^{-2}, an open circuit voltage (V_{OC}) of 1.26 V, and a fill factor (FF) of 86.56%. In addition, reliability analysis of the device was carried out using defect simulation to show how it affected the performance. The effect of the defect concentration was evaluated for Gaussian and tail-type distributions. It is interesting to note that the efficiency of the solar cell decreased from 30.59% to below 10% under a worst-case defect simulation.

1. Introduction

Renewable energy is everlasting, profitable, and sustainable. Photovoltaic (PV) technology is the most dominant across all renewable sources of energy on the market, and the crystalline silicon (c-Si)-based solar cell is the most prevalent. The availability, processing, and reliability of silicon materials are ideal for solar cells. However, the efficiency of Si solar cells reaches saturation at approximately 25%, and any further increases in efficiency are quite difficult to obtain with low-cost processing. Additionally, Si solar cells are not suitable for space applications and are limited to terrestrial applications. The above drawbacks of Si solar cells have created a platform for exploring heterojunction solar cells that can achieve the Shockley–Queisser limit at a low cost.[1]

Among thin-film PV cells, Cu–In–Ga–Se (CIGS) and Cd–Te (CdTe) are commercially available products on the market. However, the use of indium in CIGS and cadmium in CdTe is significant. Thin-film solar cells have emerged as promising alternatives to conventional silicon-based technologies. Chalcopyrite-based solar cells are cutting-edge technologies for PV use, achieving a power conversion efficiency of 20% among thin-film devices. In the class of chalcopyrite thin-film absorbers, copper gallium diselenide ($CuGaSe_2$) possesses favorable optoelectronic properties, a suitable bandgap, a high absorption coefficient, and the potential for achieving high energy conversion efficiency.

A unique feature of these materials is their exceptional radiation tolerance. In comparison to amorphous silicon solar cells, chalcopyrite devices are highly durable in space environments, reported to be up to 50 times higher. Interestingly, exposure to high doses of MeV protons and electrons has shown the potential to upgrade device capabilities in some applications. This unusual behavior is attributed to the material's intrinsic defect tolerance and its ability to undergo partial self-recovery at room temperature.[2,3]

$CuGaSe_2$ (CGS_2) possesses a bandgap of approximately 1.68 eV, which is suitable as a single junction and the top cell in tandem solar cells. $CuGaSe_2$ possesses a chalcopyrite crystal structure and is the blooming semiconductor material to be used in the absorber layer of thin-film PV cells, as well as the top cell of tandem PV cells. Because of the tunable band gap, a high observation coefficient, stability, non-toxicity, and flexibility of the tandem structure, this material is more suitable for PV applications. The lifetime of this material is 50 percent longer than that of silicon, which can be useful for terrestrial applications.

Singh *et al.* analysed the electronic, structural, optical, thermal, and elastic properties of CGSe using *Ab initio* theory and reported its material properties. Additionally, they investigated a suitable buffer layer for CGSe using CdS, ZnS, and ZnSe, and determined that the performance of CGSe increased when ZnSe was used with it, with an efficiency of 15.8%.[4] Herein, we optimized $CuGaSe_2$ and $CuInGaSe_2$ tandem solar cells with two and four terminals, achieving efficiencies of 30% under a standard AM1.5 illumination.

It is clear from the literature that the theoretical analysis of $CuGaSe_2$ is limited to ideal case simulation, but in practice, the fabricated solar cell efficiency is quite low compared to simulated results. For design engineers, the major bottleneck in simulation is to construct a practical device instead of assuming

SRM Institute of Science and Technology (Deemed to be University), Kattankulathur, Tamil Nadu 603203, India. E-mail: soumyars@srmist.edu.in

ideal conditions. Herein, we simulated an ideal device as well as a practical device by considering defects. Simulations were carried out with a wide range of defects to understand the pattern of device performance. In addition, we focused on the study of $CuGaSe_2$ to optimize the thickness of each layer (*i.e.*, absorber, buffer, window), electric field properties, recombination rate, and the four parameters of short circuit current density (J_{SC}), open circuit voltage (V_{OC}), fill factor (FF), and efficiency (EFF).

1.1. Device structure and simulation

The proposed configuration is shown in Fig. 1, and was analyzed using TCAD tool with the ZnO thickness varying from 0.1 μm to 0.2 μm, CdS thickness varying from 0.1 μm to 0.25 μm, absorber layer $CuGaSe_2$ (CGSe) thickness varying from 2 μm to 4.4 μm, and a molybdenum thickness of 0.1 μm. In this structure, the window layer is composed of ZnO due to the wider bandgap, buffer layer of CdS, and $CuGaSe_2$ (CGS_2) as the photon absorber layer. The range of thickness was taken into consideration according to the literature.[3,4]

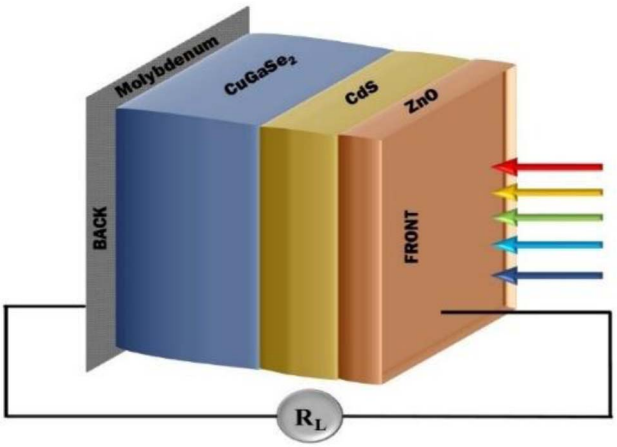

Fig. 1 Proposed device structure of the $CGSe_2$ solar cell.

The simulation was carried out with two different scenarios: (i) ideal case simulation considering negligible Shockley–Read–Hall (SRH) recombination, no surface recombination, zero interface trap density, zero bulk defect density, optimized thickness and carrier mobility, and ideal metal contacts, and (ii) practical simulation considering all types of defects and surface recombination, as discussed below. From previous studies, it is quite clear that there are different defects in CGS_2 thin film, and they are prominent in the thick layer. In this article, the presence of material defects and their effects on carrier collection and the space-charge electric field were explored in $CuGaSe_2$ (CGS_2)-based solar cells.

For a simple and understandable analysis, a metal–semiconductor ohmic contact with ideally zero resistance was considered. In practice, the contacts are non-ideal and introduce additional resistance into the equivalent circuit, which in turn reduces the fill factor of the solar cell. Ohmic contacts were used for the top and bottom contacts for the effective utilization of carriers. If there is no specification of material given by the user, the TCAD tool considers the ideal contact type with no resistance. The material's parameters for each layer of $CuGaSe_2$ (CGS_2), CdS, and ZnO are listed in Table 1 and were taken from the literature. Looking towards future generations of solar cells, a CGSe-based solar cell has the ability to achieve an efficiency greater than 30% under a standard one-sun AM1.5 illumination .[5]

The equivalent circuit diagram of a standard solar cell shows a simplified electrical equivalent model that assists researchers in increasing their understanding, analysing performance, and designing devices. It translates the physical carrier dynamics of a solar cell into an electrical component. Fig. 2(a) shows the equivalent model of a standard solar cell that is used for circuit-level analysis of contact resistance.

I_{ph} denotes the current produced by the photon excitation, I_{SH} denotes the shunt current dropped due to the shunt resistance (R_{SH}), and I_d denotes the leakage current produced by

Table 1 Material parameters used in simulation

Parameters	$CuGaSe_2$	CdS	ZnO
Thickness	**Varied**	**Varied**	**Varied**
N_A (cm^{-3})	2×10^{17}	—	—
N_D (cm^{-3})	—	1×10^{18}	1×10^{16}
E_g (eV)	1.68 (ref. 6)	2.42 (ref. 8)	3.3 (ref. 8)
μ_n ($cm^2\ V^{-1}\ s^{-1}$)	100 (ref. 6)	100 (ref. 8)	100 (ref. 8)
μ_p ($cm^2\ V^{-1}\ s^{-1}$)	50 (ref. 6)	25 (ref. 8)	25 (ref. 8)
ε	13.6 (ref. 6)	9 (ref. 8)	9 (ref. 8)
χ	3.68 (ref. 6)	4.3 (ref. 8)	4.4 (ref. 8)
N_c	2.2×10^{18} (ref. 7)	2.2×10^{18} (ref. 8)	2.2×10^{18} (ref. 8)
N_v	1.8×10^{19} (ref. 7)	1.8×10^{19} (ref. 8)	1.8×10^{19} (ref. 8)
Defect states (Gaussian and tail distribution)[8]			
N_{TD} (cm^{-3})	D: 10^{13}–10^{18}	—	—
N_{GD} (cm^{-3})	D: 10^{13}–10^{17}	—	—
W_{GD}/W_{TD} (eV)	0.05–0.25	—	—
E_{GA} (eV)		—	—
E_{GD} (eV)		—	—

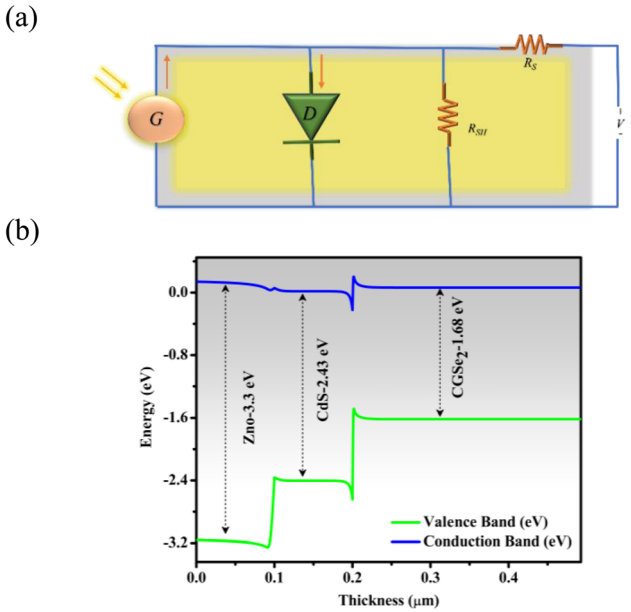

Fig. 2 (a) Equivalent circuit of a solar cell, and (b) an energy band diagram of a $CGSe_2$ solar cell.

photogenerated carrier recombination, which can be depicted using the Shockley equation for an ideal photodiode:[8]

$$I_d = I_{sh}\left(e^{\frac{V+IR_s}{nVr}} - 1\right) \quad (1)$$

The current generated by a solar cell can be represented as:

$$I = I_{ph} - I_d - I_{sh} \quad (2)$$

This equation is used to calculate the open-circuit voltage (V_{oc}) when there is zero current flow and short-circuit current (I_{sc}) with zero voltage drop across the solar cell. The fill factor (FF) is used to calculate the squareness of the J–V curve, and is expressed as the ratio of the maximum power point to I_{sc} and V_{oc}, as given below:

$$FF = \frac{P_{MAX}}{V_{oc}I_{sc}} = \frac{I_{MPP}V_{MPP}}{V_{oc}I_{sc}} \quad (3)$$

It is desired to attain a high FF for the proposed device structure, a high R_{SH} value, and low I_{SH} and R_S values to deliver the highest power to the load. Because efficiency is an integral part of the FF, optimization of a solar cell's FF can lead to enhanced device performance. In this study, the values of R_S and R_{SH} shown in Fig. 2(a) are assumed to be 0 and ∞, respectively. This analysis was performed in an ideal environment, and therefore, a comparative analysis can be accomplished. However, the device undergoes both types of resistance, which is different for different fabrication process flows. There will be a difference in fabricated device parameters compared to simulated parameters due to the consideration of ideal conditions during simulation. Therefore, the solar efficiency can be determined as follows:

$$\eta = \frac{P_{MAX}}{P_{IN}} = \frac{V_{oc}I_{sh}\cdot FF}{P_{IN}} \quad (4)$$

Fig. 2(b) shows an energy band diagram of the simulated $CGSe_2$ solar cell. The bandgap of 1.4 eV for $CGSe_2$ is used as an absorber layer, whereas other higher bandgap materials are used as window and buffer layers. Fig. 2(b) also indicates that the valence band edge of $CGSe_2$ is greater than that of CdS due to differences in electron affinity and bandgap. It smooths the flow of carriers from top to bottom. The materials are chosen so that there will be less lattice mismatch between them, which results in the formation of friendly heterojunctions.

Mathematical models include drift diffusion, the Fermi–Dirac distribution function, which is used for carrier dynamics, and Shockley–Read–Hall (SRH) and radiative recombination models are taken into consideration by Silvaco TCAD tools for recombination of carriers. The models are taken into account, considering the physical phenomenon occurring inside the heterojunction solar cell. Similar models have also been reported in numerous studies.[6–11]

Defects in a crystal are caused by the arrangement of the crystal's atomic structure during the growth process, which differs from the original structure. Defect formation is highly dynamic in nature, and kesterite materials are prone to defects due to their low-cost solution-based fabrication process flow. Hence, analysis of this type of solar cell is not accurate unless defects are properly considered. The electron can either be bound (acceptor) or released (donor) in the formation of point defects. Similarly, bulk defects are due to the presence of voids in the crystals. Defects are random in their presence, and their presence cannot be predicted.

Hence, in this analysis, the Gaussian distribution is used when the distribution of defects is undefined. This is due to the central limit theorem, which considers random variables in a state. We used the Gaussian distribution of defects across the bandgap because it can occur in a material and certainly be unknown to a designer. The tail distribution was used to examine the defect distribution along the junction or interface between heterojunctions. Hence, in this analysis, Gaussian and tail distributions were used to distribute the defects. The final density of states (DOS) of defects is shown in the model below:[12–15]

$$G(E) = G_A(E) + G_D(E)$$
$$G_A(E) = n_{TA}e^{\frac{E-E_C}{WTA}} + n_{GA}e^{-\left(\frac{E_{GA}-E}{WGA}\right)^2} \quad (5)$$
$$G_D(E) = n_{TA}e^{\frac{E_V-E}{WTD}} + n_{GA}e^{-\left(\frac{E-E_{GD}}{WGD}\right)^2}$$

The density of states of defects is shown in the model, where "A" denotes the acceptor-like state, "D" denotes the donor-like state, and "T" and "G" indicate tail distribution and

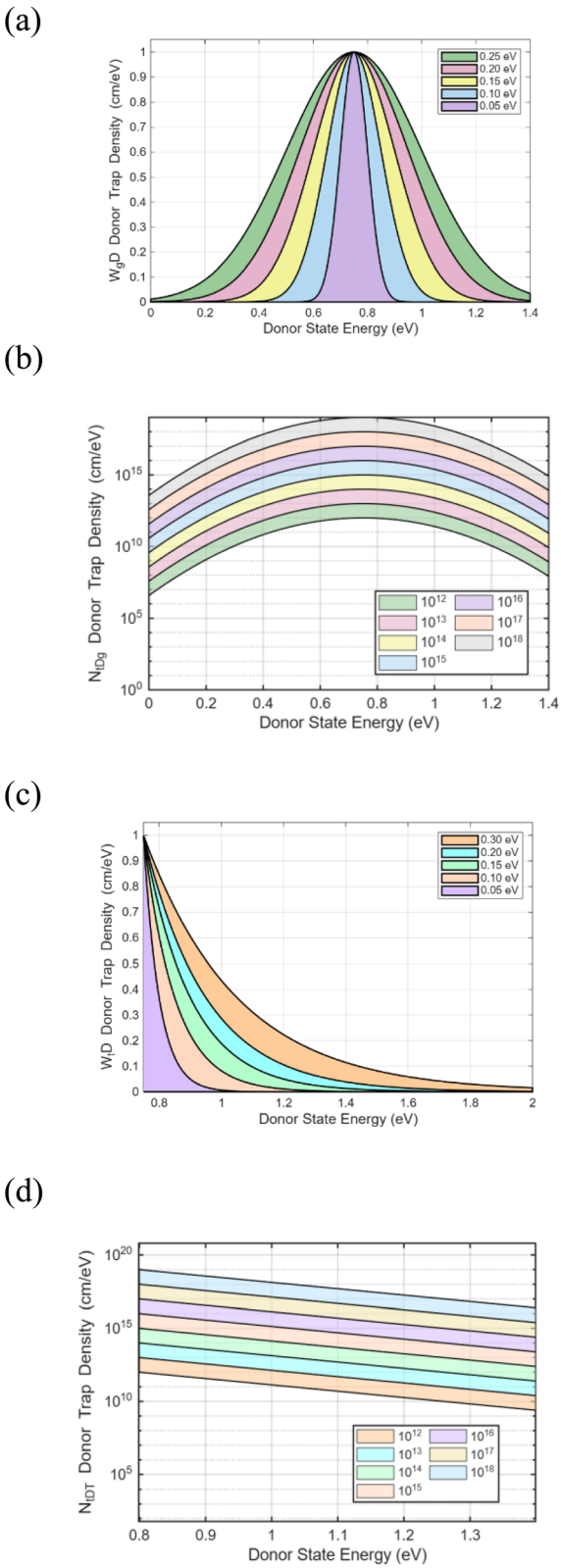

Fig. 3 Gaussian distribution with variation in (a) W_{GD} and (b) n_{GD}, and tail distribution with variation in (c) W_{TD} and (d) n_{TD}.

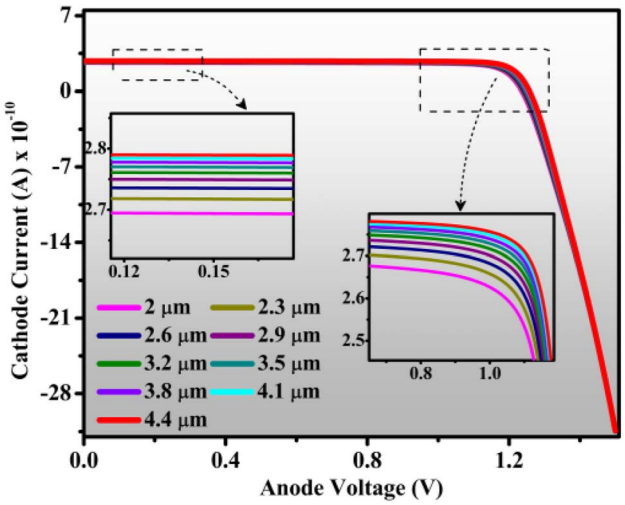

Fig. 4 *I–V* curve of the $CuGaSe_2$ absorber layer with thickness variation.

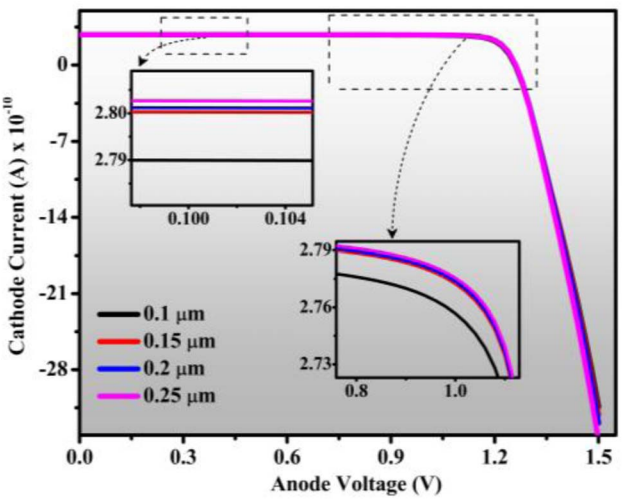

Fig. 5 *I–V* curve of the CdS buffer layer with thickness variation.

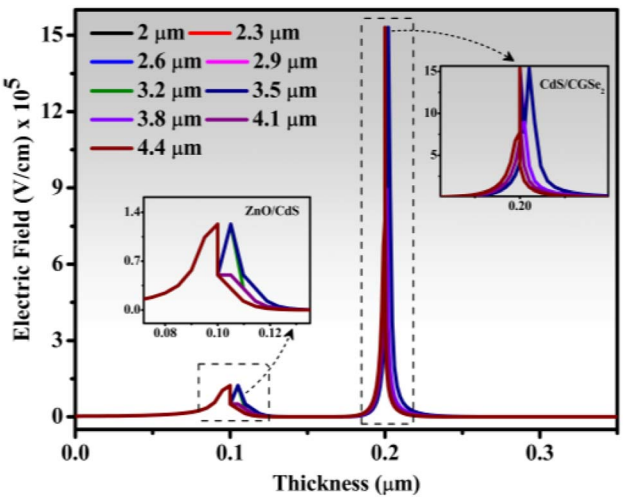

Fig. 6 Electric field curve of $CuGaSe_2$ thickness variation.

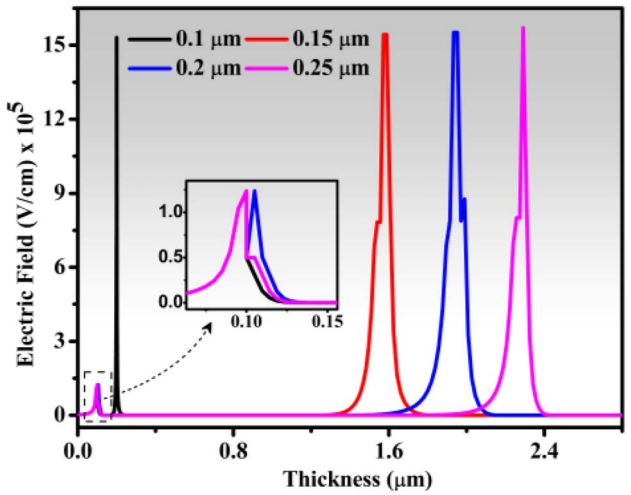

Fig. 7 Electric field curve of CdS thickness variation.

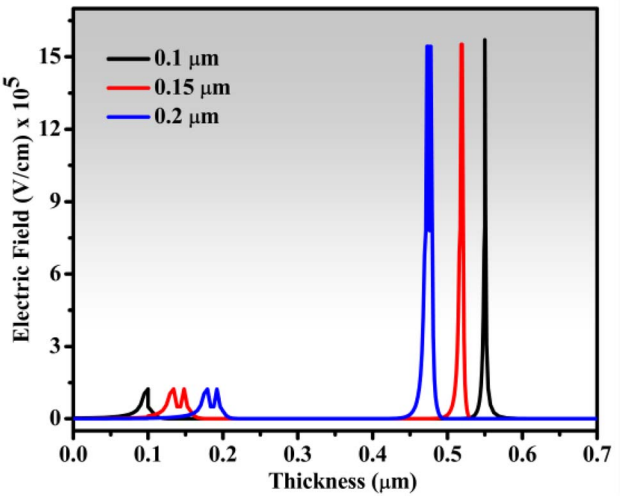

Fig. 8 Electric field curve of ZnO thickness variation.

Gaussian distribution, respectively. The tail distribution of the valence and conduction bands are represented by n_{TA} and n_{TD}, which are the intercept densities, and W_{TA} and W_{TD} represent characteristic decay energy, respectively, which together form the DOS for the exponential distribution. The DOS is the total density of states – that is, n_{GA} and n_{GD}, and its characteristic energy decay is W_{GA} and W_{GD}, with the peak energy given by E_{GD} and E_{GA} for deep defects with the Gaussian distribution, respectively. The values of n_{TD} and n_{GD} vary from 10^{13} to 10^{19}, while the values of W_{GD} and W_{TD} vary from 0.01 to 0.25, as shown in Fig. 3. The variation of density can assist a designer in understanding the range of efficiency a solar cell can achieve at different dislocation densities. In this analysis, the model of defects is more adequately explored and validated with fabricated data.[16,17]

2. Results and discussion

2.1. Dimensionality effect

The absorber layer ($CuGaSe_2$) thickness was varied from 2 μm to 4.4 μm with a doping of 2×10^{17} cm^{-3}. Fig. 4 shows the thickness variation of the absorber layer, and it is noted that an increase in the thickness of the absorber layer results in an increase in the short circuit current (I_{SC}) and open circuit voltage (V_{OC}) until it reaches 4.4 μm in thickness. Thereafter, it becomes apparent that when the curve becomes saturated, the maximum efficiency is obtained at 4.4 μm. This occurs because the carrier lifetime in bulk material performs well before optimized thickness, and carriers get recombined beyond this or face a poor collection efficiency before they have been collected by contacts.

Fig. 5 shows the thickness variation of the buffer layer (CdS), which ranges from 0.1 μm to 0.25 μm, with a fixed doping of 1×10^{18} cm^{-3} throughout the process. An increase in the buffer layer thickness resulted in an increase in efficiency from 30.1% to 30.5%. This may be due to the buffer layer thickness facilitating easy sweeping by carriers through the space-charge

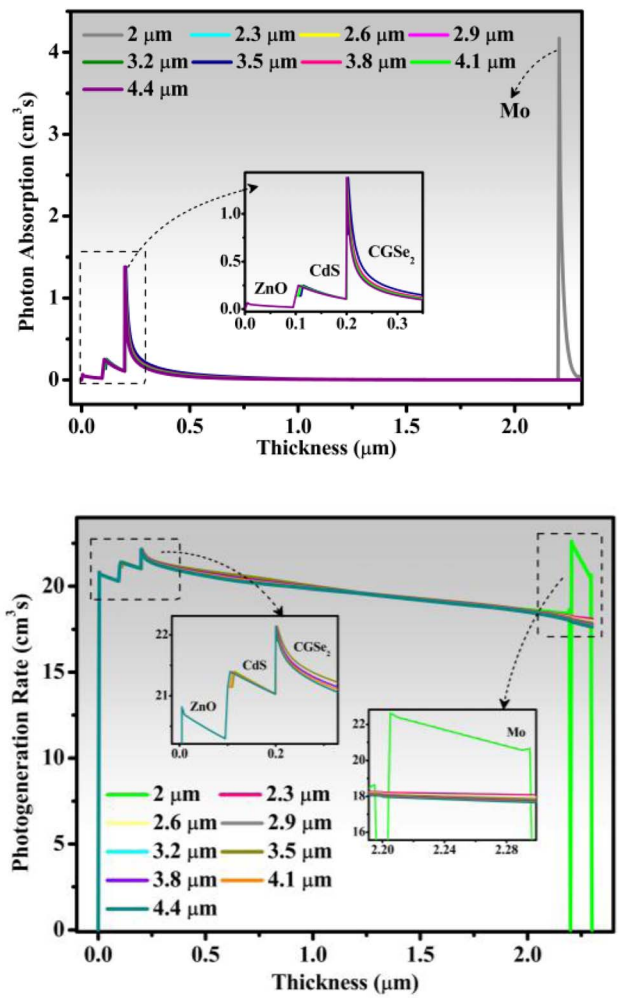

Fig. 9 Photon adsorption and photon generation rate of the $CGSe_2$ absorber layer.

region of the electric field. Upon an increase in the buffer layer beyond the optimized thickness, carriers located far from the depletion region encounter a low potential to drive through the depletion region and finally undergo recombination before collection. Hence, it is noteworthy that optimising the buffer and absorber layer can assist a designer in achieving higher efficiency as well as lower material cost.

Fig. 6 shows the electric field along the ZnO/CdS and CdS/CGSe interface. It is clearly known that the built-in electric field along these two interfaces plays a vital role in carrier separation and from the anode to the cathode. The $CuGaSe_2$ thickness variation from 2 μm to 4.4 μm can be an important point for making a perfect balance between generation and recombination of photogenerated carriers. It was noted that the electric field magnitude peaked at 3.5 μm and 4.4 μm. For this analysis, a 4.4 μm thickness was considered because its efficiency is 30.17%, which is greater than that of 3.5 μm. Thus, the reported efficiency is the ideal one when considering no defects in any layer of a solar cell.

Fig. 7 shows the effect of CdS layer thickness variation on the electric field curve. The magnitude of the electric field peak is the same for all thicknesses because when light falls on the solar cell, the photons with less energy than the CdS bandgap (2.43 eV) will be allowed to enter the buffer layer.

The physics behind this effect can be anticipated because the CdS layer behaves as a transparent layer for the wavelength, which is more than the equivalent wavelength of the CdS bandgap.

Fig. 8 shows an electric field graph of thickness variation of the ZnO layer, ranging from 0.1–0.2 μm. It was observed that the formation of the two heterojunctions of ZnO/CdS and CdS/$CuGSe_2$ has a very minimal effect on the electric field of the solar cell.

When the electric field magnitude peaks at 0.1 μm, this occurs because when light falls on the cell, the photons with less energy than the CdS buffer layer (3.3 eV) will be allowed into the adsorber layer, and others will be reflected back. The ZnO layer in this solar cell is mostly used as a window layer to capture additional photons of higher wavelength and provide the CdS/$CuGSe_2$ interface with a sufficient platform to separate additional photogenerated carriers into photocurrent. Hence, it was observed that the variation in thickness of the ZnO buffer layer will not greatly affect the efficiency. The major electric field effect on the performance of the solar cell in Fig. 6 is due to the absorber layer thickness variation. The results are quite in accordance with the physics behind solar cell carrier dynamics.

Fig. 9 shows the photon adsorption and photon generation rate of the $CGSe_2$ absorber layer, which touches the peak at the $CGSe_2$ layer.

This occurs because the absorption coefficient of $CGSe_2$ is high, and it absorbs most of the photons from sunlight. It is also worthy to mention that light is absorbed in a few nanometers of the absorber layer, which results in a high photon absorption and photon generation rate near the $CGSe_2$ layer of the cell, and then decreases over the thickness of the absorber layer. Because molybdenum is used as a back contact, it reflects the light into the $CGSe_2$ absorber layer, and this reflection causes a high peak in the absorption and generation rate in the molybdenum interface.

Fig. 10 shows the performance-measuring parameters of $CuGaSe_2$ for solar cells, which are J_{SC}, V_{OC}, FF, and efficiency

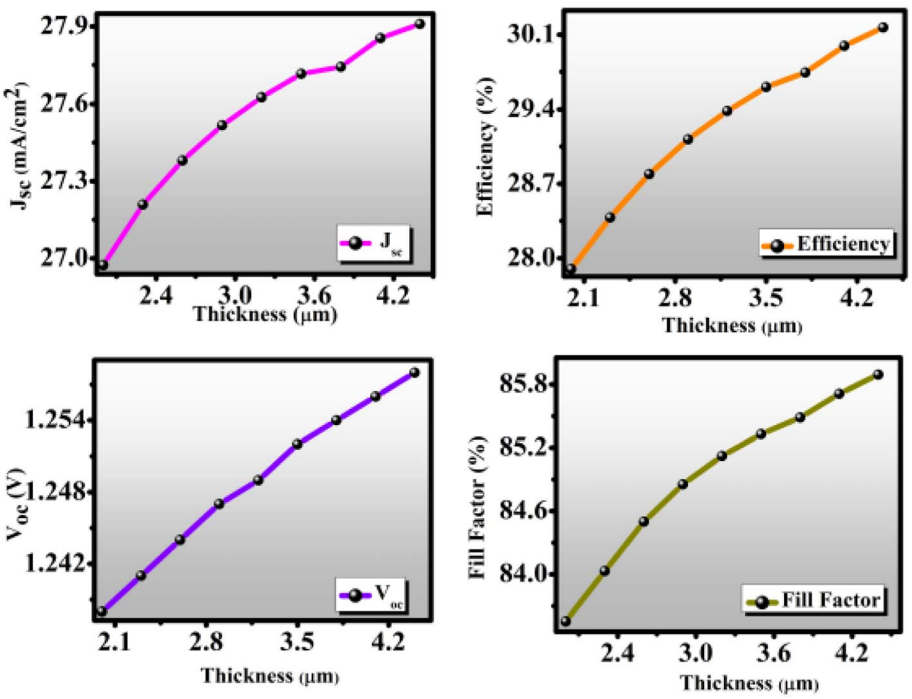

Fig. 10 J_{SC}, V_{OC}, FF, and η of $CuGaSe_2$ of the solar cell over thickness.

(η). The thickness of the absorber layer ($CuGaSe_2$) increased from 2 μm to 4.4 μm, and short circuit current density (J_{SC}) and open circuit voltage (V_{OC}) increased to 4.4 μm. Beyond

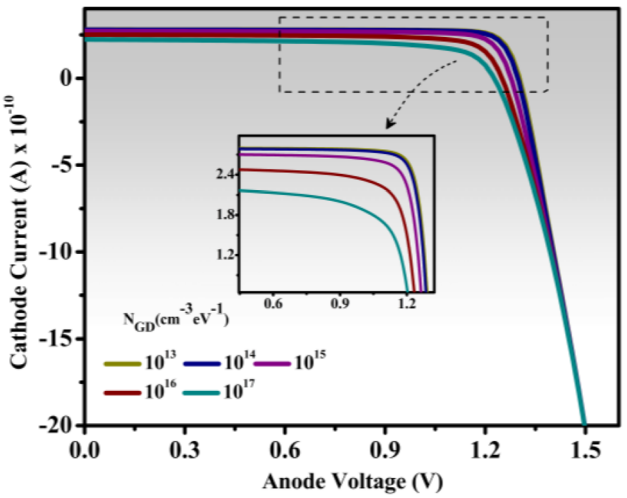

Fig. 11 *I–V* characteristics of solar cells under defect density variation of the Gaussian distribution.

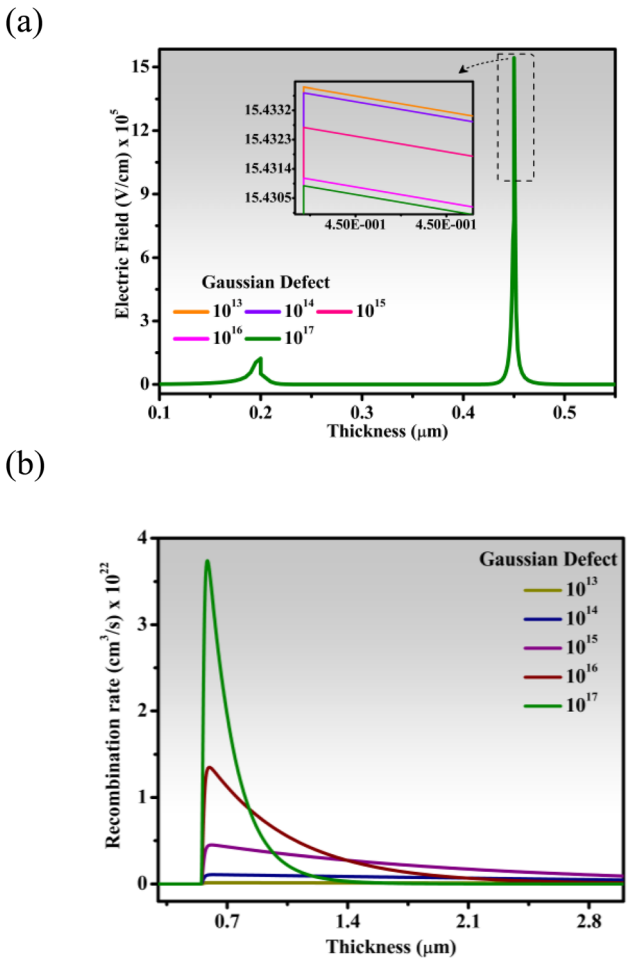

Fig. 12 (a) Electric field curve and (b) recombination rate of the defect density variation of the Gaussian distribution.

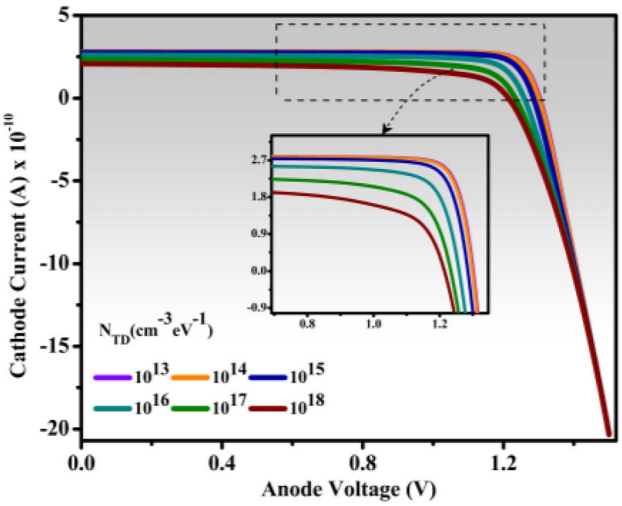

Fig. 13 *I–V* characteristics of defect density variation of the tail distribution.

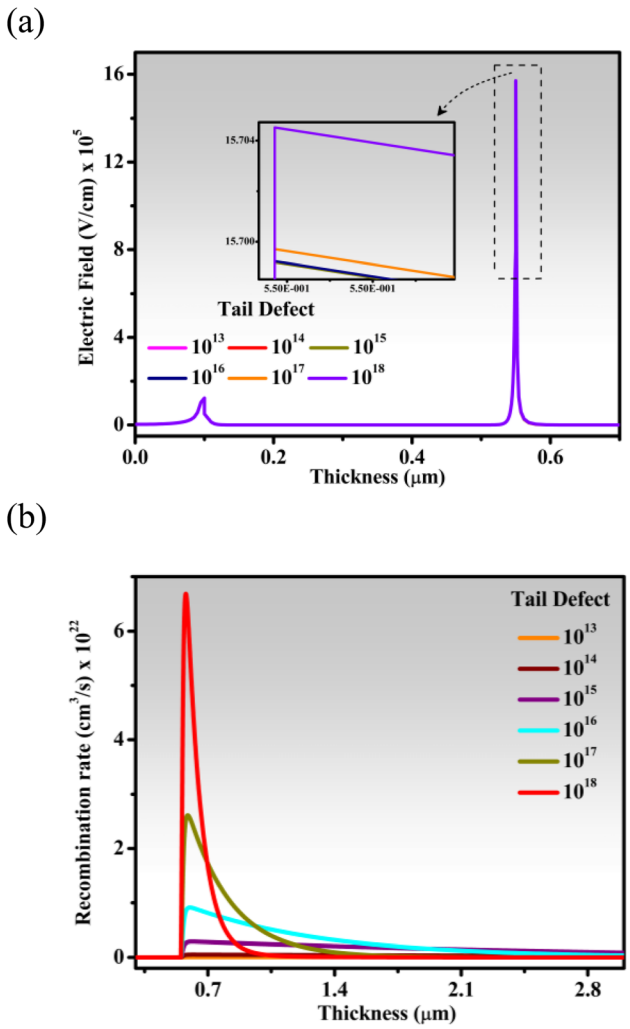

Fig. 14 (a) Electric field curve and (b) recombination rate of defect density variation of the tail distribution.

this thickness, J_{SC} and V_{OC} begin to saturate due to the increase in thickness. The efficiency (η) also increased from 27.9% to 30.1% at 2 μm to 4.4 μm thickness, respectively. For the maximum thickness of 4.4 μm, an FF of 85.89% was recorded.

2.2. Effect of defect concentration in the absorber layer

It is well-known that chalcogen materials are prone to defects, which mainly arise due to vacancies, antisites, interstitials, and defect complexes in the bulk layer. These defects create unwanted energy vacancies inside the material bandgap, causing shallow defects and deep trap level states. These defects then cause faults or reliability concerns in the atomic structure of the material. In part A of this study, the performance of the solar cell was evaluated considering the ideal material properties, such as no defects. However, in practice, the scenario is quite different, and the absorber material behaves as an epicentre for many types of defects.

In this study, the performance of solar cells was analyzed under different defect states, which not only examines the reliability issues of solar cells but also provides clarity to practical solar cell performance. In simulation, $CuGaSe_2$ is assumed to have donor-type defects, which consist of Gaussian defects and tail defects.

The main reason for considering the Gaussian and tail distribution of defects is the unavailability of experimental data on the distribution types of these defects in the literature. Hence, for simulation instead of random distribution, Gaussian and tail distribution functions were used for a proper analysis. A Gaussian distribution occurs when the defect is concentrated in the middle of the bandgap, and a tail-type distribution occurs when the defect is spread over the edge. These defects were varied from 10^{13}–10^{17} eV^{-1} and 10^{13}–10^{18} eV^{-1}, respectively, to determine how the optical and electrical properties of solar cells are affected.

2.2.1. Gaussian distribution. The Gaussian defects represent intrinsic bulk defects in film that are due to native point defects such as Cu vacancies, Ga vacancies, and antisite defects that arise when film grows in a non-stoichiometric ratio. It results in deep or mid-gap states that serve as Shockley–Read–Hall recombination centers in solar cells. The SRH recombination model was incorporated to consider this effect. When the defect density increases, it affects the performance of solar cells. Fig. 11 shows the *I–V* curve of defect variations of Gaussian density, which have been varied from 10^{13}–10^{17} cm^{-3} eV^{-1}. The increase in defect density will lead to decreases in the performance of the solar cell due to greater recombination or shorter carrier lifetime.

Fig. 12(a) shows the electric field distribution for the solar cells with Gaussian defect densities that have been varied from 10^{13}–10^{17}. The graph shows two heterojunctions, which are the ZnO–CdS junction and the CdS–$CuGaSe_2$ junction. It is noted

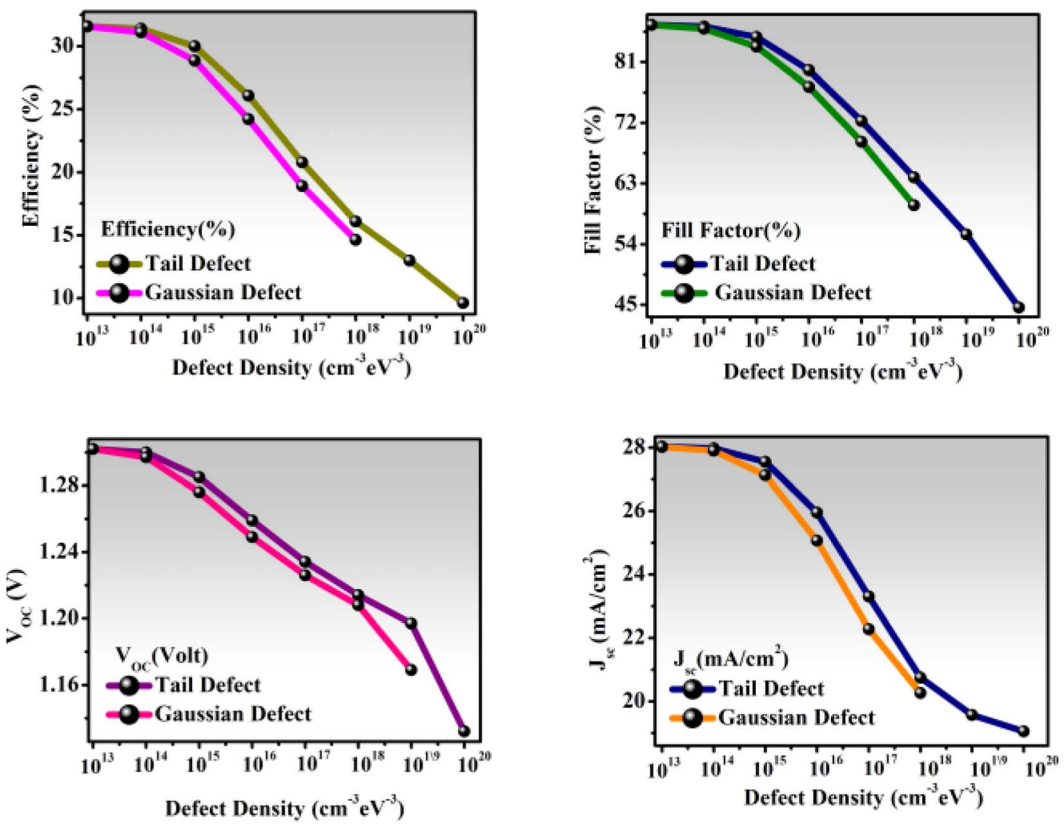

Fig. 15 J_{SC}, V_{OC}, FF, and efficiency of the absorber layer defect density variation.

that the peak of the CdS–$CuGaSe_2$ junction is higher than that of the ZnO–CdS junction. Fig. 12(b) shows the recombination rate (RR). There is greater recombination for higher n_{GD} values at the CdS–$CuGaSe_2$ junction, and *vice versa*.

2.2.2. Tail distribution. The tail-type (exponential) defect distribution is for defects that are caused by the material itself, such as band-edge fluctuations and grain-boundary states, and these are physically linked to the band-tailing generated by improper composition and lattice disorder. Fig. 13 shows the *I–V* curve of defect density variation for the tail distribution, which was varied from 10^{13}–10^{18} cm^{-3} eV^{-1}. It was found that an increase in defect density will result in a decrease in the performance of the solar cell. Fig. 14(a) shows the electric field distribution of the solar cell with tail defect densities. Fig. 14(b) shows the recombination rate (RR). Higher n_{TD} values result in greater recombination at the CdS–$CuGaSe_2$ junction, and *vice versa*.

Fig. 15 shows how the variation in Gaussian defect density and tail defect density affects the solar cell parameters (*i.e.*, short circuit current (J_{SC}), open circuit current (V_{OC}), fill factor (FF), and efficiency (EFF) curve). The density of the Gaussian and tail defects varies from 10^{13}–10^{17} cm^{-3} eV^{-1} and 10^{13}–10^{18} cm^{-3} eV^{-1}, respectively.

This graph shows that an increase in defect density results in a decrease in the parameters, which occurs due to additional defects affecting the recombination of carriers. This recombination of carriers occurs in the absorber layer of solar cells.

2.3. Effect of defect concentration with width variation in the absorber layer

Defect density variation results in changes in the number of defects (N_D). The shape of the defect (*i.e.*, Gaussian or tail distribution) was fixed, and only the height was increased, which was previously discussed. The defect density distribution with width variation was performed to determine how defect states are spread across energy levels. Thus, the simulation results can be matched with the real-time fabrication results.

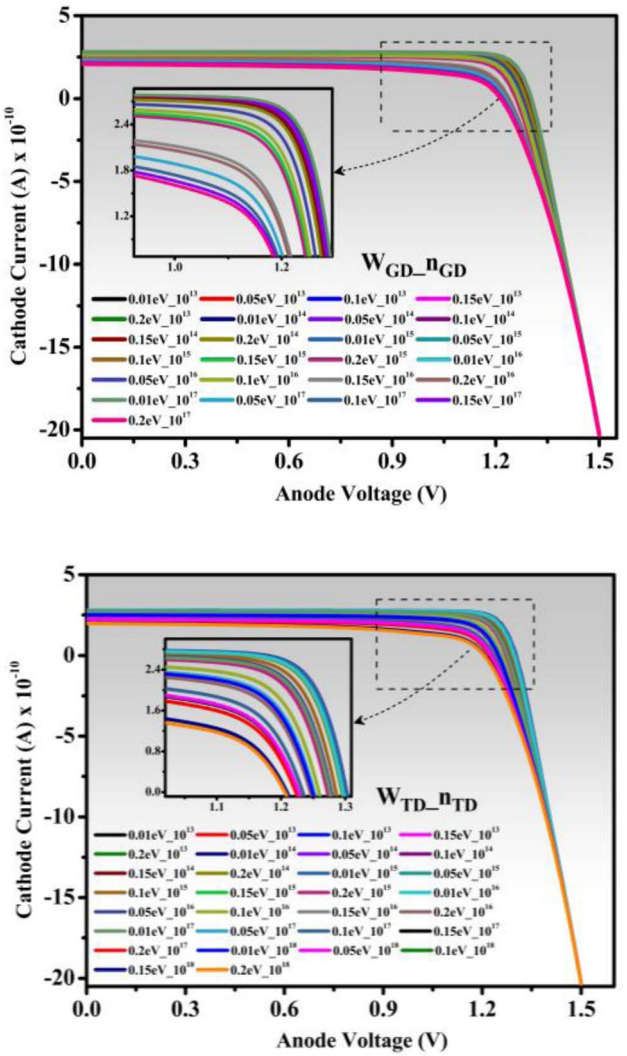

Fig. 16 *I–V* characteristics of defect density and width variation of the Gaussian and tail distribution.

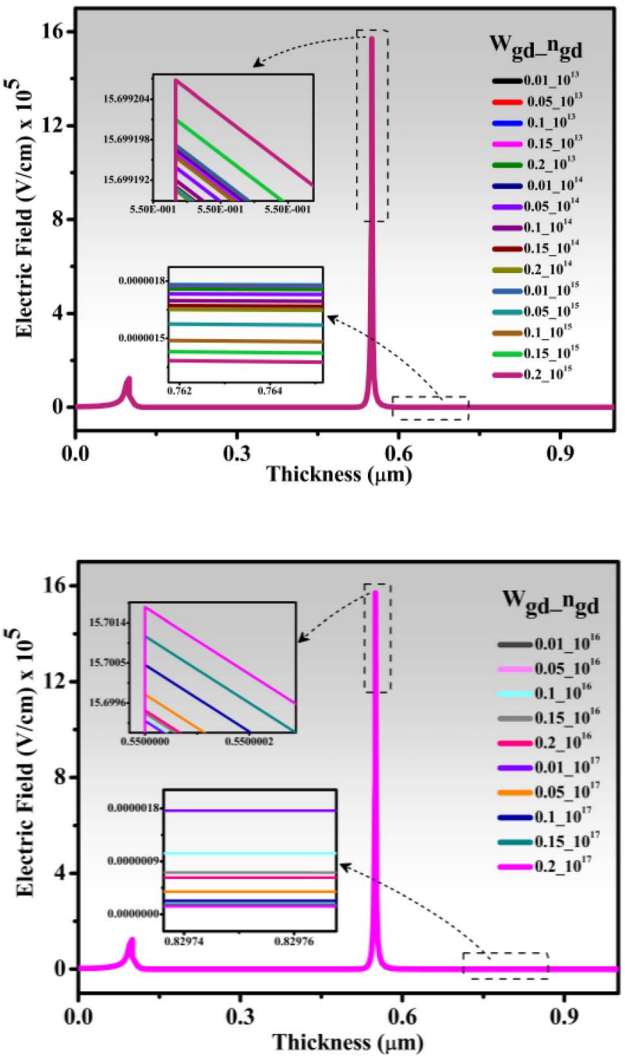

Fig. 17 Electric field curve of the defect density and width variation of the Gaussian distribution.

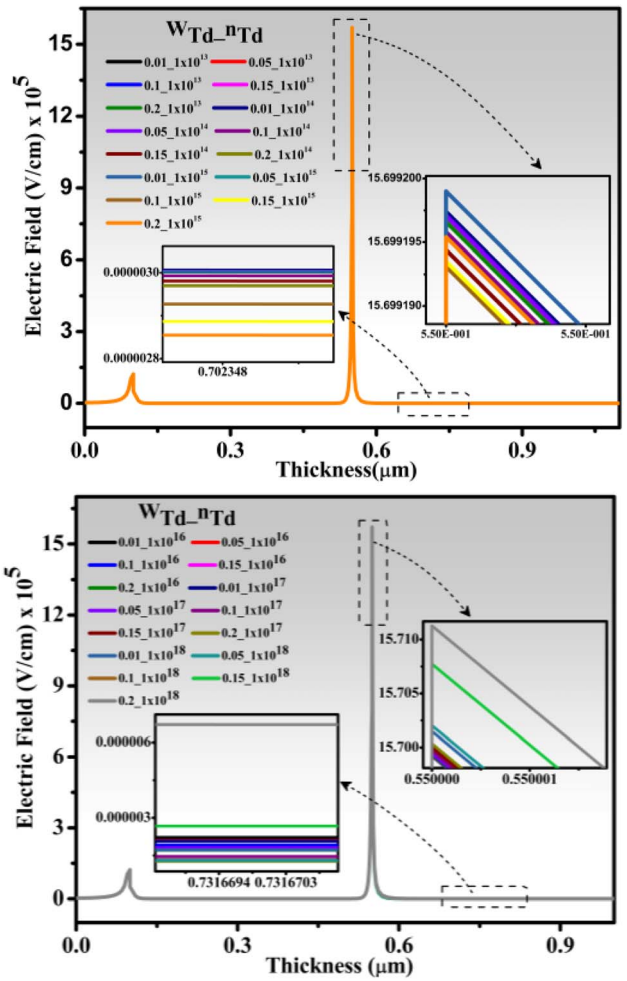

Fig. 18 Electric field curve of the defect density and width variation of the tail distribution.

Fig. 16 shows the Gaussian defect density (n_{GD}) from 10^{13}–10^{17} cm^{-3} eV^{-1} for W_{GD} in the range of 0.01–0.2 eV. An increase in the defect density and width variation resulted in a decrease in the short-circuit current and open-circuit voltage. This was due to additional defects resulting in greater recombination of carriers, which indicates that photogenerated carriers are wasted before being collected.

Fig. 17 and 18 show the electric field curve of defect density and width variation of Gaussian and tail distributions with values of 10^{13}–10^{17} cm^{-3} eV^{-1}, 0.05–0.25 eV and 10^{13}–10^{18} cm^{-3} eV^{-1}, 0.05–0.25 eV, respectively. It was observed that there is a formation of two heterojunction layers of ZnO/CdS and CdS/$CuGSe_2$. It was noted that the magnitude of the peak of the CdS–$CuGaSe_2$ junction was higher than that of the ZnO–CdS junction.

Fig. 19 presents the effect of defect density and width variation of the Gaussian distribution on J_{SC}, V_{OC}, FF, and EFF with a corresponding increase in the Gaussian density from 10^{13}–10^{17} cm^{-3} eV^{-1} and width variation from 0.05–0.25 eV. There was a decrease in all parameters with increasing defect density. With increasing defect density, there were decreases in the potential (J_{SC}) from 28 to 20 mA cm^{-2}, the fill factor (FF) from 86 to 64, and the efficiency (EFF) from 31 to 16.1% for different values of W_{GD}.

Fig. 20 shows the effect of defect density and width variation of the tail distribution on J_{SC}, V_{OC}, FF, and EFF with a corresponding increase in tail density from 10^{13}–10^{18} cm^{-3} eV^{-1} and width variation from 0.05–0.25 eV. For all four parameters, there was a decrease with increasing defect density, with a decrease in potential (J_{SC}) from 28 to 19 mA cm^{-2}, fill factor (FF) from 86 to 59, and efficiency (EFF) from 30.59% to 9.6% for different values of W_{TD}. It is clear from this analysis that a fabricated device can achieve an efficiency of at least 9.6% in a worst case scenario, which was also reported in the literature.[10]

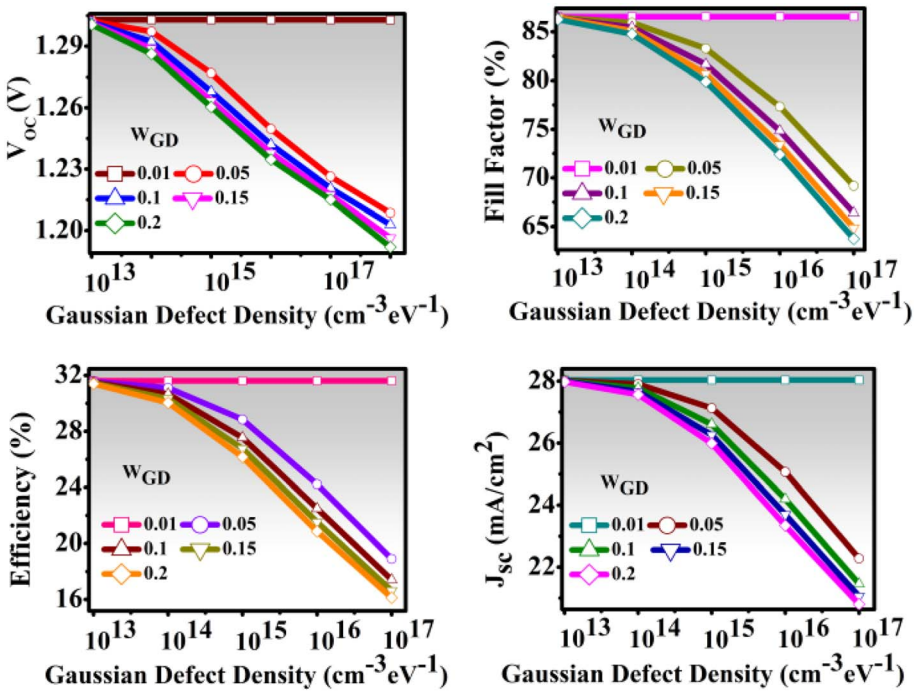

Fig. 19 J_{SC}, V_{OC}, FF, and efficiency of the defect density and width variation of the Gaussian distribution.

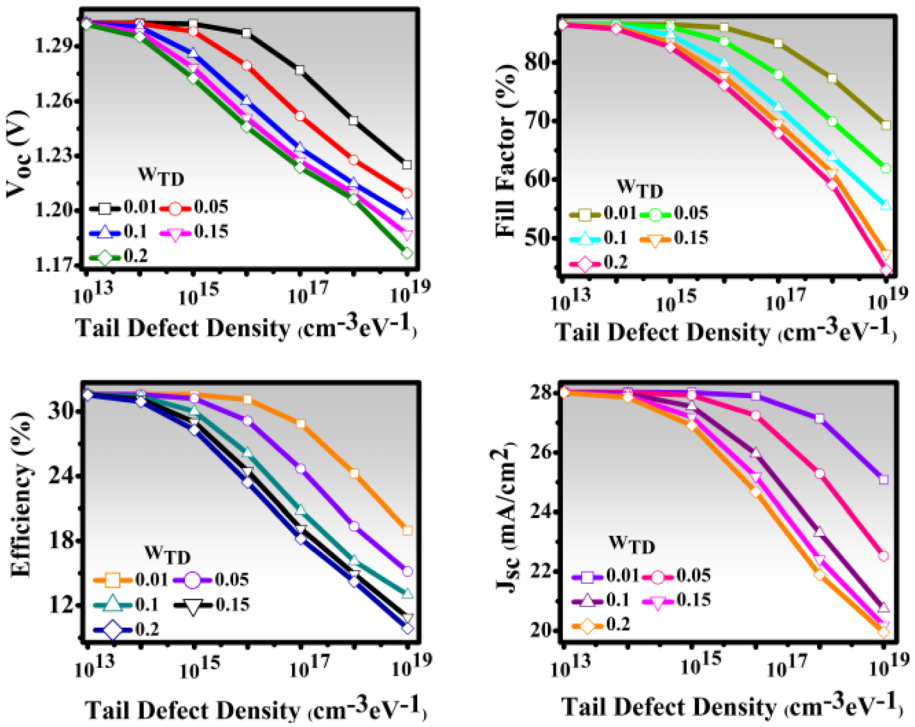

Fig. 20 J_{SC}, V_{OC}, FF, efficiency of defect density, and width variation of the tail distribution.

3. Conclusion

This work represents an in-depth analysis of next-generation thin-film solar cells with an absorber layer of $CuGaSe_2$. Optimization of device dimensions was carefully carried out to ensure optimized device performance. The performance of the device was analyzed with the support of physics behind the device, such as a built-in electric field, potential, and most importantly, the recombination rate. The models of the device were chosen in accordance with the working phenomenon of solar cells during simulation. The dimensions of ZnO, CdS, and $CuGaSe_2$ were optimized at 0.1 μm, 0.25 μm, and 4.4 μm, respectively. For an optimized ZnO, CdS, and $CuGaSe_2$ layer, the J_{SC} value was 28.03 mA cm^{-2}, the V_{OC} was 1.26 V, the efficiency (η) was 30.59%, and the fill factor (FF) was 86.56%. A reliability analysis of the solar cells under various defect densities was also performed. It is quite interesting to observe that the performance of the solar cell decreased to less than 10% under a higher defect density. This analysis brings new insight to the future fabrication of solar cells.

Conflicts of interest

There is no conflicts to declare.

Data availability

The data for this article, including codes, are available upon reasonable request to the authors.

References

1 B. Saha, B. K. Mondal, S. K. Mostaque, M. Hossain and J. Hossain, Numerical Modeling of CUSBSE2-based dual-heterojunction thin film solar cell with CGS back surface layer, *AIP Adv.*, 2023, **13**(2), 025255, DOI: 10.1063/5.0133889.
2 F. Werner, *et al.*, Ultra-thin passivation layers in Cu(In,Ga)Se_2 thin-film solar cells: Full-area passivated front contacts and their impact on bulk doping, *Sci. Rep.*, 2020, **10**(1), 7530, DOI: 10.1038/s41598-020-64448-9.
3 M. Elbar, S. Tobbeche and A. Merazga, Effect of top-cell CGS thickness on the performance of CGS/CIGS tandem solar cell, *Sol. Energy*, 2015, **122**, 104–112, DOI: 10.1016/j.solener.2015.08.029.
4 P. Singh, R. Gautam, S. Sharma, S. Kumari and A. S. Verma, Simulated solar cell device of $CuGaSe_2$ by using CdS, ZnS and ZnSe buffer layers, *Mater. Sci. Semicond. Process.*, 2016, **42**, 288–302, DOI: 10.1016/j.mssp.2015.10.030.
5 J. Arunachalam and K. Sivaperuman, An investigation of the influence of various factors on the electrical performance of a ($CuGaS_2$) -based thin-film solar cell using SCAPS-1D software, *Optik*, 2024, **303**, 171744, DOI: 10.1016/j.ijleo.2024.171744.
6 J. Jiang, *et al.*, Optimization bandgap gradation structure simulation of $Cu_2Sn_{1-x}Ge_xS_3$ solar cells by SCAPS, *Sol. Energy*, 2019, **194**, 986–994, DOI: 10.1016/j.solener.2019.11.014.
7 J. M. T and E. K, Numerical simulation for optimal thickness combination of cds/zns dual buffer layer cuingase2 solar cell

using SCAPS 1D, *Indian J. Sci. Technol.*, 2019, **12**(45), 01–06, DOI: 10.17485/ijst/2019/v12i45/148395.

8 P. G. Kumar, P. Chandrasekar, S. Routray, M. Courel and Y. Massoud, Understanding performance limitation of CuCdSnS as photoactive layer: Physics of defect states and recombination mechanisms, *IEEE Sens. J.*, 2022, **22**(21), 20381–20388, DOI: 10.1109/jsen.2022.3205661.

9 W.-K. Chen, *Linear Networks and Systems*, Wadsworth, Belmont, CA, USA, 1993, pp. 123–135.

10 G. O. Young, "Synthetic structure of industrial plastics", in *Plastics*, ed. J. Peters, McGraw-Hill, New York, NY, USA, 2nd edn, 1964, vol. 3, pp. 15–64.

11 ATLAS User's Manual, *Silvaco Int.*, Santa Clara, CA, USA, 2015.

12 A. Zekry, A. Shaker and M. Salem, "Solar cells and arrays", *Advances in Renewable Energies and Power Technologies*, 2018, pp. 3–56, DOI: 10.1016/b978-0-12-812959-3.00001-0.

13 S. Torres-Jaramillo, A. Morales-Acevedo, R. Bernal-Correa and A. Pulzara-Mora, Optimizing two and four-terminal CuGaSe2/CuInGaSe2 tandem solar cells for achieving high efficiencies, *Optik*, 2018, **175**, 71–77, DOI: 10.1016/j.ijleo.2018.08.12.

14 L. Sravani, S. Routray, K. P. Pradhan and M. C. Piedrahita, Kesterite thin-film solar cell: Role of grain boundaries and defects in copper–zinc–tin–sulfide and copper–zinc–tin–selenide, *Phys. Status Solidi A*, 2021, **218**(16), 2100039, DOI: 10.1002/pssa.202100039.

15 L. Sravani, S. Routray, M. Courel and K. P. Pradhan, Loss mechanisms in CZTS and CZTSE kesterite thin-film solar cells: Understanding the complexity of defect density, *Sol. Energy*, 2021, **227**, 56–66, DOI: 10.1016/j.solener.2021.08.052.

16 J. A. Joya, M. A. Hossain, K. Chakma and S. Hussain, Numerical Study of Chalcopyrite N-$CuAlSe_2$/p-$CuGaSe_2$ solar cell with an additional $CuTiTe_2$ back absorber layer using a SCAPS-1D simulator and machine learning approach, *Semicond. Sci. Technol.*, 2026, **41**(2), 025006, DOI: 10.1088/1361-6641/ae3f4b.

17 M. Elbar and S. Tobbeche, Numerical simulation of CGS/CIGS single and tandem thin-film solar cells using the Silvaco-Atlas Software, *Energy Procedia*, 2015, **74**, 1220–1227, DOI: 10.1016/j.egypro.2015.07.766.